PAPER

CrossMark
click for updates

Cite this: DOI: 10.1039/c4dt02336f

Smaller than a nanoparticle with the design of discrete polynuclear molecular complexes displaying near-infrared to visible upconversion†‡

Davood Zare,[a] Yan Suffren,[b] Laure Guénée,[c] Svetlana V. Eliseeva,[d] Homayoun Nozary,[a] Lilit Aboshyan-Sorgho,[a] Stéphane Petoud,*[d] Andreas Hauser*[b] and Claude Piguet*[a]

This work shows that the operation of near-infrared to visible light-upconversion in a discrete molecule is not limited to non-linear optical processes, but may result from superexcitation processes using linear optics. The design of nine-coordinate metallic sites made up of neutral N-heterocyclic donor atoms in kinetically inert dinuclear $[GaEr(L1)_3]^{6+}$ and trinuclear $[GaErGa(L2)_3]^{9+}$ helicates leads to $[ErN_9]$ chromophores displaying unprecedented dual visible nanosecond $Er(^4S_{3/2} \rightarrow {}^4I_{15/2})$ and near-infrared microsecond $Er(^4I_{13/2} \rightarrow {}^4I_{15/2})$ emissive components. Attempts to induce one ion excited-state absorption (ESA) upconversion upon near-infrared excitation of these complexes failed because of the too-faint Er-centred absorption cross sections. The replacement of the trivalent gallium cation with a photophysically-tailored pseudo-octahedral $[CrN_6]$ chromophore working as a sensitizer for trivalent erbium in $[CrEr(L1)_3]^{6+}$ improves the near-infrared excitation efficiency, leading to the observation of a weak energy transfer upconversion (ETU). The connection of a second sensitizer in $[CrErCr(L2)_3]^{9+}$ generates a novel mechanism for upconversion, in which the superexcitation process is based on the Cr^{III}-sensitizers. Two successive $Cr \rightarrow Er$ energy transfer processes (concerted-ETU) compete with a standard Er-centred ETU, and a gain in upconverted luminescence by a factor larger than statistical values is predicted and observed.

Introduction

Compared to the classical spontaneous transformation of energy in physics (energy degradation) and in chemistry (spontaneous chemical reactions induced by negative free energy

[a]Department of Inorganic and Analytical Chemistry, University of Geneva, 30 quai E. Ansermet, CH-1211 Geneva 4, Switzerland. E-mail: Claude.Piguet@unige.ch
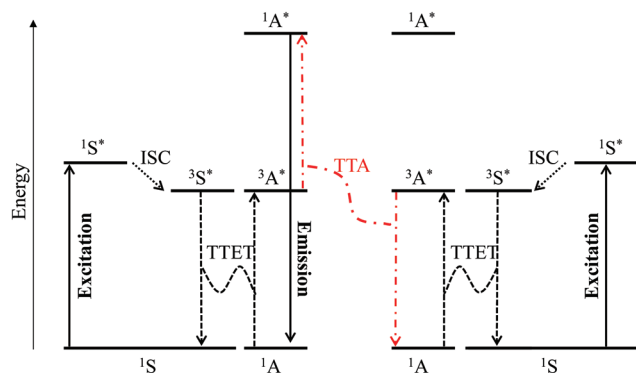[b]Department of Physical Chemistry, University of Geneva, 30 quai E. Ansermet, CH-1211 Geneva 4, Switzerland. E-mail: Andreas.Hauser@unige.ch
[c]Laboratory of Crystallography, University of Geneva, 24 quai E. Ansermet, CH-1211 Geneva 4, Switzerland
[d]Centre de Biophysique Moléculaire, CNRS UPR 4301, Rue Charles Sadron, F-45071 Orléans Cedex 2, France. E-mail: Stephane.Petoud@inserm.fr

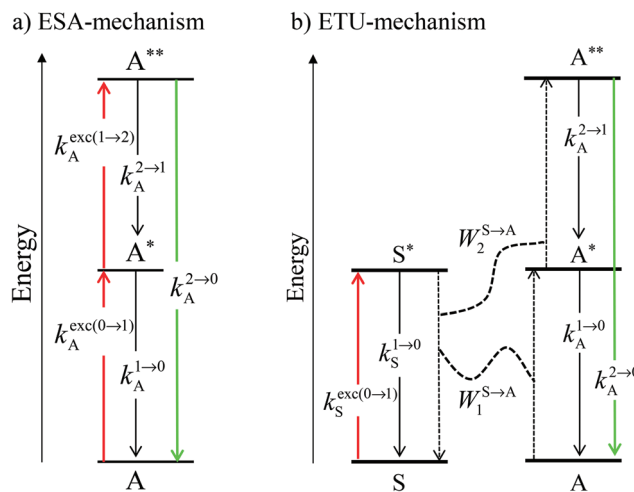† Submitted to *Dalton Transactions* dedicated themed issue: Advancing the chemistry of the f-elements.

‡ Electronic supplementary information (ESI) available: Synthesis of ligand **L1** (Appendix 1), determination of thermodynamic exchange constants (Appendix 2), kinetic analysis (Appendix 3) and calculation of normalized steady-state population densities (Appendix 4). Tables collecting elemental analysis (Table S1), ESI-MS peaks (Tables S2–S3) and crystallographic data (Tables S4–S5). Figures showing NMR spectra (Fig. S1–S4), ORTEP views (Fig. S5), packing interactions (Fig. S6–S8) and photophysical data (Fig. S9–S25). CCDC 1003567 and 1003568. For ESI and crystallographic data in CIF or other electronic format see DOI: 10.1039/c4dt02336f

changes), near-infrared (NIR) to visible light-upconversion processes may appear puzzling. However, it has been known for a long time that the intense electromagnetic irradiation (typically in the range of MW cm^{-2}) of polarizable materials may induce weak non-linear responses, which ultimately produce photons of higher energy than those used for excitation.[1] Despite the low quantum yields of such non-linear processes, the transparency of living tissues to incident NIR light was attractive enough to exploit these phenomena for the *in vivo* sensitization of optical probes and sensors in photobiology.[2] For technological applications, such huge input intensities are of limited interest, and efforts are directed towards the design of upconverting materials based on linear optical processes and compatible with common light sources, for instance for the conversion of the NIR part of the solar light into green emission compatible with its absorption by dye-sensitized or by crystalline silica solar cells (the power-density of the terrestrial solar irradiance is approximately 0.1 W cm^{-2}).[3]

In this context, the non-coherently sensitized upconversion based on triplet–triplet annihilation (TTA) is currently one of the most efficient strategies.[4] According to the mechanism depicted in Scheme 1, a sensitizer (S)/acceptor (A) pair of molecules is required. The sensitizer S is responsible for the

Scheme 1 Qualitative Jablonski diagrams illustrating the sensitized triplet–triplet annihilation (TTA) upconversion process operating in a S/A mixture. Solid arrows indicate transitions in which a photon is involved, while black dashed arrows indicate radiationless processes (ISC = inter-system crossing and TTET = triplet–triplet energy transfer). The alternating dashed-dotted red arrows stand for the triplet–triplet annihilation mechanism.

Scheme 2 Kinetic schemes depicting the modelling of activator-centred superexcitation processes according to (a) a one ion excited state absorption (ESA) process and (b) an energy transfer upconversion (ETU) process occurring upon off-resonance excitations. $k_A^{exc(0\to1)}$ and $k_S^{exc(0\to1)}$ are the pumping rate constants for the irradiation into the activator, respectively sensitizer absorption bands, $k_A^{i\to j}$ and $k_S^{i\to j}$ are the decay rate constants (i.e. the sum of radiative and non-radiative processes) of level i into level j centred on the sensitizer and on the activator, respectively. $W_n^{S\to A}$ are the rate constants of sensitizer-to-activator energy transfer processes. Red solid arrows correspond to excitation photons and green solid arrows stand for upconverted emission.

^{1}S→^{1}S* light-harvesting process which is followed by an intersystem crossing (ISC) process leading to the establishment of a long-lived triplet excited state ^{3}S*. The subsequent ^{3}S*/^{1}A→^{1}S/^{3}A* Dexter-type triplet–triplet energy transfer provides an acceptor-centred triplet state ^{3}A*, which is sufficiently long-lived to diffuse and to collide with a second partner. The triplet–triplet annihilation then produces a mixture of singlet, triplet and quintet excited dimers, in which the ^{3}A* + ^{3}A*→^{1}A* + ^{1}A pathway leads to the targeted high-energy singlet excited state on the acceptor. Relaxation of the ^{1}A* state to the ground state is finally accompanied by the emission of a photon of higher energy than those involved in the excitation process. Typical green-to-blue upconversion is experimentally observed by using sensitizers and activators containing aromatic ring systems of various sizes. However, the requirements for the diffusion and collision of two excited triplet acceptors for TTA limit this methodology to intermolecular processes occurring in solution, in rubbery polymeric materials or in solid matrices, ensuring sufficiently efficient diffusion of molecules and/or molecular excitons under anaerobic conditions (since dioxygen can easily quench triplet excited states).[4]

Though less efficient in terms of quantum yields, the superexcitation mechanisms depicted in Scheme 2 also rely on linear and sequential optical processes. They are currently implemented in low-phonon nanoparticles,[5] but their engineering can be theoretically further miniaturized and confined in a single molecular entity. For the one ion excited state absorption mechanism (ESA, Scheme 2a), the initial excitation produces an intermediate excited state, the lifetime of which must be long enough to allow for a second absorption process to occur. Such a situation is difficult to implement in molecules where the existence of high-energy oscillators drastically reduces the excited-state lifetimes.[6] Indeed, attempts to detect ESA-processes in coordination complexes using trivalent lanthanides as activators (Ln = Er, Tm, Yb) have failed to date,[7] except for a very recent report claiming that NIR to visible ESA-

upconversion could be detected upon very intense irradiation of dimethylsulfoxide solutions containing Tm^{3+}.[8] Indirect excitation using sensitizers for collecting the initial NIR irradiation followed by energy transfer onto the acceptor (ETU, Scheme 2b) may benefit from the larger absorption cross sections and longer lifetimes of the sensitizers,[5] but to date only little attention has been given to the implementation of ETU in molecules. In 2003, Hoshino and coworkers reported a surprising linear Er-centred upconversion process induced by the intense irradiation of the low-energy tail of the ligand-absorption band in films of [Er(quinolinate)$_3$] complexes, but its alternative assignment to a ligand-centred non-linear optical two-photon absorption followed by Er-centred luminescence could not be excluded.[9] Inspired by this pioneering work, Piguet and co-workers used trivalent chromium for the indirect sensitization of Er^{III} in the trinuclear triple-stranded [CrErCr(**L2**)]$^{9+}$ helicate.[10] Continuous-wave NIR irradiation at 750 nm indeed generated the excitation of the chromium cations via their spin-flip Cr(^{2}E←^{4}A$_2$) and Cr(^{2}T$_1$←^{4}A$_2$) transitions, which were responsible for a weak, but reproducible green upconverted erbium-centred Er(^{4}S$_{3/2}$→^{4}I$_{15/2}$) luminescence at 540 nm (Scheme 3).[10] The quadratic dependence of the upconverted emission upon the incident intensity observed in diluted solutions combined with the crucial role played by Cr→Er energy transfer processes unambiguously support the presence of an ETU mechanism operating within a single supramolecular complex.[11]

Further optimization requires a deeper level of understanding of the ETU mechanism in [CrErCr(**L2**)]$^{9+}$. This work can be
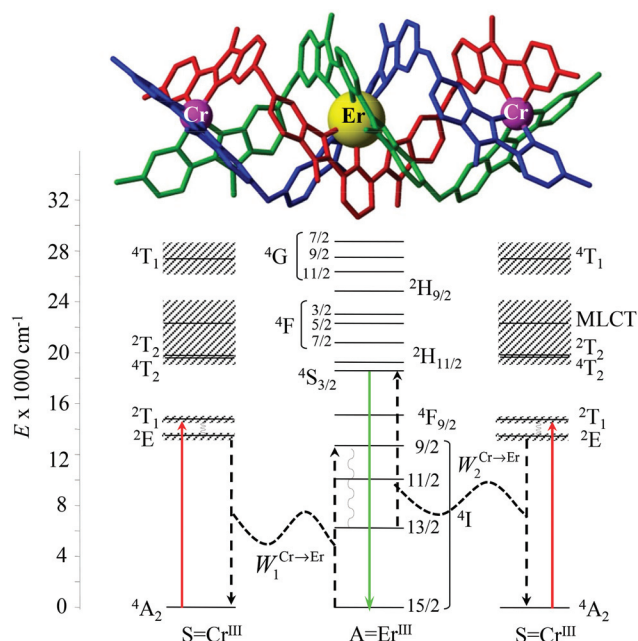
Scheme 3 Jablonski diagrams obtained from absorption and emission spectra recorded for the different chromophores in [CrErCr(**L2**)₃]-(CF₃SO₃)₉. Black dashed arrows indicate radiationless sensitizer-to-activator energy transfer processes and curled arrows stand for non-radiative internal conversion. Red solid arrows correspond to the NIR excitation photons and the green solid arrow stands for the visible upconverted emission. Adapted from ref. 11.

achieved thanks to the preparation of analogous complexes, in which (i) the photophysically active Cr^{III} and Er^{III} chromophores are replaced by 'innocent' partners and (ii) the number of Cr-sensitizers per Er-activators is increased stepwise from 0 to 2. Here we thus report on the chemical strategy used for the design of isostructural polynuclear heterometallic gallium–lanthanide and chromium–lanthanide complexes, in which energy transfer upconversion can be deciphered and optimized.

Results and discussion

Optimizing the erbium coordination sphere for its use as an activator in molecular upconversion processes

Except for the report of Hoshino and co-workers, who assigned not less than ten emission bands to Er-centred luminescence upon ligand excitation in the [Er(quinolinate)₃] complexes,[9] a behaviour that is reminiscent to that found for Er-doped solids,[12] we are not aware of the description of any erbium coordination complex displaying a luminescence signal other than the 1.5 μm band attributed to the Er($^4I_{13/2} \rightarrow {}^4I_{15/2}$) transition.[13] This observation agrees with the large weighted average effective vibrational energy of ~2000 cm^{-1} participating in the non-radiative relaxation processes for lanthanide complexes containing organic ligands.[7] For Er^{III}, the reduced energy gap p (in phonons units) between adjacent levels hardly exceeds $p = 2$ and the dominant nonradiative relaxation pre-

vents luminescence in coordination complexes, except for the fluorescence of the lowest Er($^4I_{13/2}$) excited state for which $p \geq 3$.[7]

Efforts made for protecting the erbium-activator from high-energy C–H oscillators in coordination complexes succeeded in extending the Er($^4I_{13/2}$) excited state lifetimes by more than one order of magnitude,[13i] and we therefore planned to take advantage of this strategy with the introduction of rigid unsaturated bis-(N-methyl-benzimidazol-2-yl)pyridine tridentate units **L0** into the segmental ligands **L1** and **L2** (Scheme 4, see Appendix 1 in the ESI‡). Reaction of **L0** with Ln(CF₃SO₃)₃ was known to give poorly stable triple-helical [Ln(**L0**)₃]$^{3+}$ complexes with the small Y^{3+} and Er^{3+} cations,[14] but the formation of these [LnN₉] chromophores was favoured by the self-assembly of **L1** and **L2** with Ln(CF₃SO₃)₃ in the presence of Ga(CF₃SO₃)₃. The heterometallic dinuclear [GaLn(**L1**)₃](CF₃SO₃)₆·mC₂H₅CN·nH₂O and trinuclear [GaLnGa(**L2**)₃](CF₃SO₃)₉·mC₂H₅CN·nH₂O
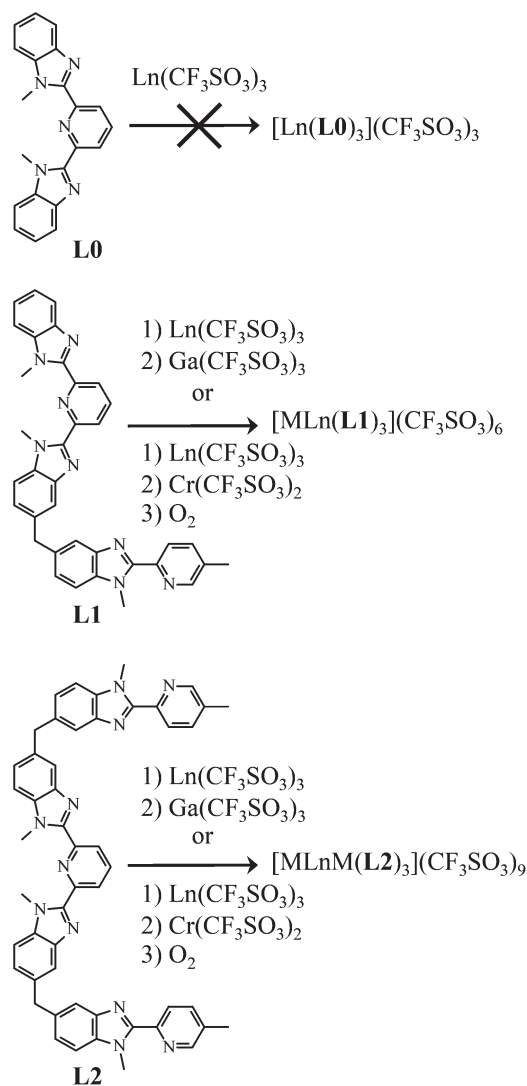
Scheme 4 Chemical structures of ligands **L0**–**L2** and preparation of the dinuclear [MLn(**L1**)₃](CF₃SO₃)₆ and trinuclear [MLnM(**L1**)₃](CF₃SO₃)₉ helicates (M = Ga, Cr and Ln = Ho, Er, Tm, Y).

helicates could be isolated in 40–90% yields (Scheme 4 and Table S1 in the ESI‡).

ESI-MS data unambiguously establish the charge balance between $[GaLn(L1)_3]^{6+}/6CF_3SO_3^-$ and $[GaLnGa(L2)_3]^{9+}/9CF_3SO_3^-$ (Tables S2–S3 in the ESI‡) whereas the ^1H NMR spectra collected for the diamagnetic Ga^{3+}/Y^{3+} pair in acetonitrile at submillimolar concentrations confirmed the self-assembly of stable C_3-symmetrical $[GaY(L1)_3]^{6+}$ (Fig. S1 in the ESI‡) and D_3-symmetrical $[GaYGa(L2)_3]^{9+}$ complexes (Fig. S2 in the ESI‡), for which the unusual upfield chemical shifts of the aromatic protons H6 and H9 together with the diastereotopic splitting of H7 and H8 were diagnostic for the twisted arrangement of the ligand strands in these triple-stranded helicates (Fig. 1).[15] Upon addition of one equivalent of paramagnetic $Eu(CF_3SO_3)_3$ into an acetonitrile solution of $[GaYGa(L2)_3]^{9+}$, the ^1H NMR spectrum remained unchanged for months at room temperature, thus demonstrating the exceptional kinetic inertness of these trinuclear helicates (Fig. S3 in the ESI‡). In contrast, the trivalent lanthanide coordinated in the dinuclear $[GaY(L1)_3]^{6+}$ complex was more accessible to metal exchange, and the replacement of Y^{3+} with Eu^{3+} according to the equili-

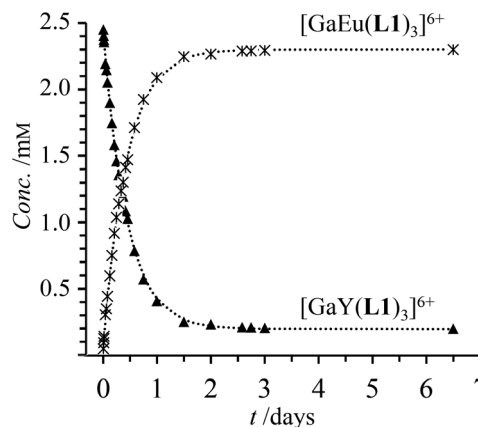**Fig. 2** Kinetic traces monitored by ^1H NMR for the reaction of [GaY(L1)₃](CF₃SO₃)₆ (1.0 eq.) with Eu(CF₃SO₃)₃ (1.0 eq.) at 293 K. The dotted lines correspond to the best exponential fits.

brium (1) could be monitored on the timescale of hours (Fig. 2 and S4 in the ESI‡).

$$[GaY(L1)_3]^{6+} + Eu^{3+} \rightleftharpoons [GaEu(L1)_3]^{6+} + Y^{3+} \quad K_{exch}^{Y,Eu} \quad (1)$$

$$K_{exch}^{Y,Eu} = \frac{\beta_{1,1,3}^{Ga,Eu,L1}}{\beta_{1,1,3}^{Ga,Y,L1}} = \frac{[GaEu]_{eq.}[Y]_{eq.}}{[GaY]_{eq.}[Eu]_{eq.}} \quad (2)$$

The integration of the ^1H NMR signals at chemical equilibrium gave $K_{exch}^{Y,Eu} = 134(3)$ according to eqn (2), from which a stabilization factor of $\xi = \log(K_{exch}^{Y,Eu}) = \log(\beta_{1,1,3}^{Ga,Eu,L1}) - \log(\beta_{1,1,3}^{Ga,Y,L1}) = 2.13(1)$ was deduced for the replacement of a small Y^{3+} with a midrange size Eu^{3+} cation in the nine-coordinate cavity found in $[GaLn(L1)_3]^{6+}$. The $\beta_{1,1,3}^{Ga,Ln,L1}$ stands for the cumulative formation constants of the $[GaLn(L1)_3]^{6+}$ complexes, while $[GaLn]_{eq.}$ and $[Ln]_{eq.}$ correspond to the equilibrium concentrations of complexes and free metals (a standard concentration $c^\theta = 1.0$ m is taken for the reference state, see Appendix 2 in the ESI‡). This trend is remarkable when one considers the minute $\Delta R_{CN=9}^{Y\rightarrow Eu} = 0.045$ Å increase in the lanthanide nine-coordinate ionic radius, but it is in line with $\xi = 1.3(2)$ reported for the replacement of Ln = Ho^{3+} with Ln = Gd^{3+} in $[Ln(L0)_3]^{3+}(\Delta R_{CN=9}^{Ho\rightarrow Gd} = 0.035$ Å).[14c] Since no significant quantity of intermediate complexes could be detected by ^1H NMR during the exchange reaction (Fig. S4‡), reaction (1) could be tentatively considered as a reversible second-order elementary reaction, for which the quadratic rate law is given by

$$-\frac{d[GaY]}{dt} = [GaY]^2(k_f - k_r) + [GaY]\{k_f([Eu]_{tot} - [Ga]_{tot}) + k_r([Y]_{tot} + [Ga]_{tot})\} - k_r[Ga]_{tot}[Y]_{tot} \quad (3)$$

where k_f and k_r stand for the forward and backward second-order rate constants, respectively (see Appendix 3 in the ESI‡).[16] However, the observation of mono-exponential kinetic traces for both [GaY] depletion and [GaEu] rising with a common rate constant $k = 2.3(1) \times 10^{-5}$ s^{-1} ($\tau_{1/2} = \ln(2)/k = 8.3(4)$ hours, Fig. 2) suggests the more complicated mechan-
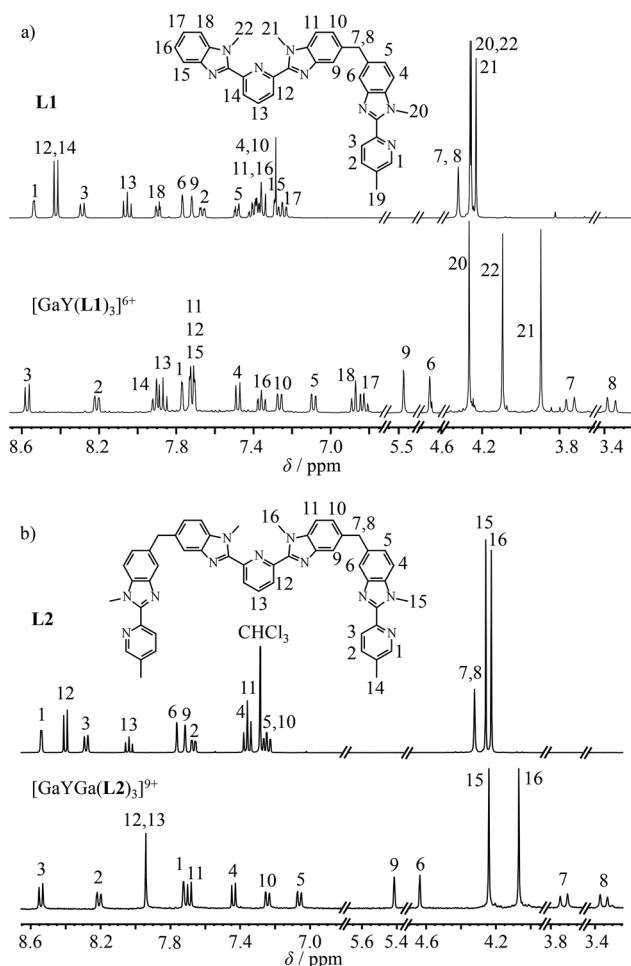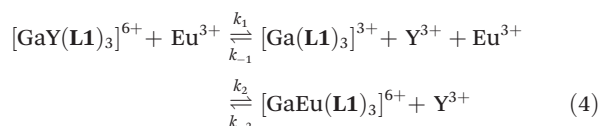

Fig. 1 ^1H NMR spectra with assignment for (a) **L1** and [GaY(L1)₃]⁶⁺ and (b) **L2** and [GaYGa(L2)₃]⁹⁺ at 293 K (in CDCl₃ for the ligands and in CD₃CN for the complexes).

ism shown in eqn (4), in which the first-order dissociation processes characterized by k_1 and k_{-2} values are the rate limiting steps.[17]

$$[GaY(L1)_3]^{6+} + Eu^{3+} \underset{k_{-1}}{\overset{k_1}{\rightleftharpoons}} [Ga(L1)_3]^{3+} + Y^{3+} + Eu^{3+}$$

$$\underset{k_{-2}}{\overset{k_2}{\rightleftharpoons}} [GaEu(L1)_3]^{6+} + Y^{3+} \qquad (4)$$

We conclude that the non-covalent cryptate $[GaYGa(L2)_3]^{9+}$ is sufficiently inert ($\tau_{1/2} > 1$ month) to be used as a host matrix for diluting isomorphous and photophysically active $[GaErGa(L2)_3]^{9+}$, $[CrYCr(L2)_3]^{9+}$ or $[CrErCr(L2)_3]^{9+}$ complexes using co-crystallization. In contrast, $[GaY(L1)_3]^{6+}$ is too labile ($\tau_{1/2} = 8.3(4)$ hours) for accommodating $[CrEr(L1)_3]^{6+}$ guests without undergoing lanthanide exchange processes.

Slow diffusion of *tert*-butylmethylether into an acetonitrile solution of $[GaErGa(L2)_3]^{9+}$ provided prisms of $[GaErGa(L2)_3]$-$(CF_3SO_3)_9(CH_3CN)_{35.5}$, the crystal structure of which (Fig. S5‡) is isostructural with those reported for $[CrLnCr(L2)_3]$ $(CF_3SO_3)_9(C_2H_5CN)_{30}$ (Ln = Eu, Yb, Fig. 3 and Table S4‡).[10] The close packing of the triple-helical cations $[GaErGa(L2)_3]^{9+}$ in the crystal produces large interstitial cavities, which are filled with disordered counter-anions and solvent molecules (Fig. S6–S7‡). The erbium atom is coordinated by nine heterocyclic nitrogen atoms occupying the vertices of a distorted tricapped trigonal prism. We were unable to obtain X-ray quality crystals for $[GaEr(L1)_3](CF_3SO_3)_6$, but the slow diffusion of *tert*-butylmethylether into a concentrated propionitrile solution of $[CrEr(L1)_3]^{6+}$ succeeded in crystallizing the analogous dinuclear $[CrEr(L1)_3](CF_3SO_3)_6(C_3H_5N)_{26}$ complex. The $[CrEr(L1)_3]^{6+}$ cations are packed in columns with opposite helicities along the crystallographic threefold axes passing through the metal ions (Fig. 4a, S8 and Table S5‡). In line with the rigidity of the polyaromatic strands, the intermetallic distance Cr⋯Er = 8.704(1) Å found in $[CrEr(L1)_3]^{6+}$ compares well with those found in the trinuclear analogue (Ga1⋯Er1 = 8.974(1) Å and Er1⋯Ga2 = 8.887(1)Å). The superimposition of the triple-helical cations $[CrEr(L1)_3]^{6+}$ with $[GaErGa(L2)_3]^{9+}$ further demonstrates similar triple-helical organizations (Fig. 4b).

The photophysical properties confirmed the structural similarities, and ligand-centred excitation at $\lambda_{ex} = 405$ nm ($\bar{\nu}_{exc} =$

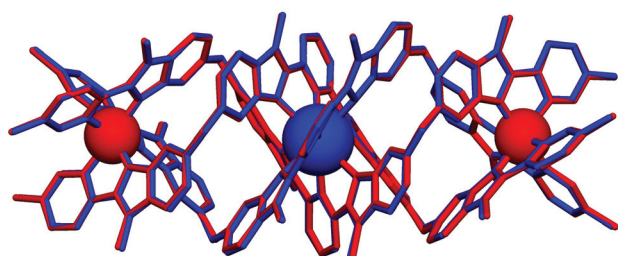Fig. 3 Superimposition of the molecular structures of $[GaErGa(L2)_3]^{9+}$ (red) and $[CrEuCr(L2)_3]^{9+}$ (blue) observed in the crystal structures of $[GaErGa(L2)_3](CF_3SO_3)_9(CH_3CN)_{35.5}$ and $[CrEuCr(L2)_3](CF_3SO_3)_9(C_2H_5-CN)_{30}$.[10] The hydrogen atoms are omitted for clarity.

a)

b)

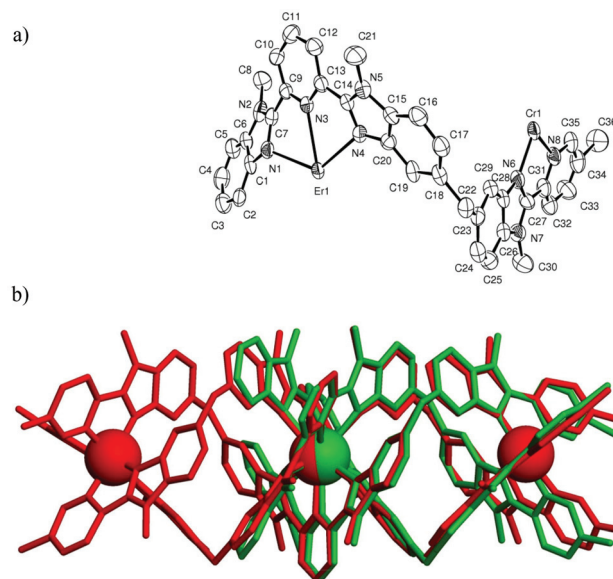

Fig. 4 (a) ORTEP view with the numbering scheme of the asymmetric unit in the crystal structure of $[CrEr(L1)_3](CF_3SO_3)_6(C_3H_5N)_{26}$. Ellipsoids are represented at the 30% probability level and hydrogen atoms are omitted for clarity. (b) Superimposition of the molecular structures of $[CrEr(L1)_3]^{6+}$ (green) and $[GaErGa(L2)_3]^{9+}$ (red).

Table 1 Characteristic excited state lifetimes (τ) and associated rate constants ($k = \tau^{-1}$) measured for $[CrLn(L1)_3](CF_3SO_3)_6$ and $[CrLnCr(L2)_3]$-$(CF_3SO_3)_9$ in the solid state at 10 K[a]

	$[CrLn(L1)_3]^{6+}$	$[CrLnCr(L2)_3]^{9+}$
$\tau_{Cr}^{1 \to 0}(Cr_nY)/s$	$2.767(10) \times 10^{-3}$	$2.336(10) \times 10^{-3}$
$k_{Cr}^{1 \to 0}(Cr_nY)/s^{-1}$	362(1)	428(2)
$\tau_{Er}^{1 \to 0}(Ga_nEr)/s$	$4.28(2) \times 10^{-6}$	$1.5(1) \times 10^{-6}$
$k_{Er}^{1 \to 0}(Ga_nEr)/s^{-1}$	$2.34(1) \times 10^5$	$6.7(4) \times 10^5$
$\tau_{Er}^{2 \to 0}(Ga_nEr)/s$	$3.8(4) \times 10^{-8}$	$4.0(2) \times 10^{-8}$
$k_{Er}^{obs}(Ga_nEr)/s^{-1}$	$2.6(3) \times 10^7$	$2.5(1) \times 10^7$
$k_{Er}^{2 \to 0}(Ga_nEr)/s^{-1}$	1.615×10^{3b}	1.615×10^{3b}
$k_{Er}^{2 \to 1}(Ga_nEr)/s^{-1}$	$2.6(3) \times 10^{7c}$	$2.5(1) \times 10^{7c}$
$W_1^{Cr \to Er}(Cr_nEr)/s^{-1}$	295(5)	170(4)

[a] $k_{Cr}^{1 \to 0}$, $k_{Er}^{1 \to 0}$ and $k_{Er}^{obs}(Ga_nEr) = 1/\tau_{Er}^{2 \to 0}(Ga_nEr) = k_{Er}^{2 \to 1} + k_{Er}^{2 \to 0}$ are the decay rate constants (*i.e.* the sum of radiative and non-radiative processes) of the Cr(^{2}E$\to^4$A$_2$) transitions measured in Cr$_n$Y, and of the Er(^{4}I$_{13/2} \to ^4$I$_{15/2}$) and Er(^{4}S$_{3/2} \to ^4$I$_{15/2}$) transitions measured in Ga$_n$Er, respectively. $W_1^{Cr \to Er}$ are the rate constants for the Cr(^{2}E)$\to$Er(^{4}I$_{9/2}$) energy transfer processes. [b] $k_{Er}^{2 \to 0} = \left(\tau_{Er,rad}^{^4S_{3/2}} \right)^{-1} = (619 \,\mu s)^{-1}$ is taken as the Er(^{4}S$_{3/2}$) radiative lifetime measured for Er^{3+}-doped into yttrium aluminium garnet.[21] [c] $k_{Er}^{2 \to 1}(Ga_nEr) = k_{Er}^{obs}(Ga_nEr) - k_{Er}^{2 \to 0}$.

24 691 cm^{-1}) of solid-state samples of $[GaEr(L1)_3](CF_3SO_3)_6$ and $[GaErGa(L2)_3](CF_3SO_3)_9$ displayed a standard ligand-to-erbium energy transfer followed by NIR emission signals centred at 6500 cm^{-1} assigned to the split Er(^{4}I$_{13/2} \to ^4$I$_{15/2}$) transition.[11] The roughly temperature-independent monoexponential lifetimes found for the Er(^{4}I$_{13/2}$) excited state (3.1(4) μs for GaEr and 4.1(3) μs for GaErGa between 10 and 293 K, entries 3 and 4 in Table 1 and Fig. S9‡) combined with the detection of additional green Er(^{4}S$_{3/2} \to ^4$I$_{15/2}$) emission
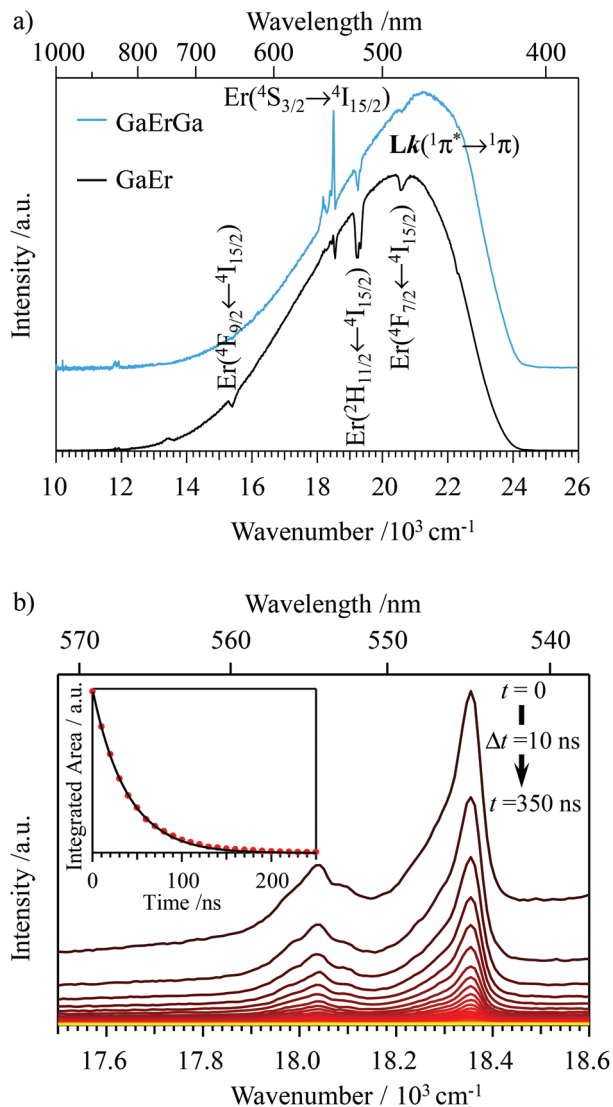
Fig. 5 (a) Luminescence spectra recorded for $[GaEr(L1)_3](CF_3SO_3)_6$ (the black trace) and $[GaErGa(L2)_3](CF_3SO_3)_9$ (the blue trace) at 3 K in the solid state (λ_{ex} = 405 nm or $\bar{\nu}_{exc}$ = 24 691 cm^{-1}, cutoff filter 420 nm). The dips correspond to internal Er-centred re-absorption of ligand-centred emission.[13g] (b) Time-resolved luminescence spectra recorded between t = 0 and t = 350 ns (Δt = 10 ns) and luminescence decay trace (inset) recorded for the $Er(^4S_{3/2} \rightarrow {}^4I_{15/2})$ transition in $[GaErGa(L2)_3](CF_3SO_3)_9$ at 3 K in the solid state (λ_{ex} = 405 nm or $\bar{\nu}_{exc}$ = 24 691 cm^{-1}, cut-off filter 420 nm). The black curve corresponds to the best exponential fit applied to the decay points deduced from the integration of the intensity traces of the $Er(^4S_{3/2} \rightarrow {}^4I_{15/2})$ transition.

centred at λ_{em} = 542 nm in both complexes ($\bar{\nu}_{em}$ = 18 450 cm^{-1}, Fig. 5a and S10‡) reflect the exceptional protection of the erbium cation from interactions with high-energy phonons and vibrations in these $[ErN_9]$ chromophores.[11,18] Though technically challenging (see the Experimental section), the kinetic traces of the Er-centred green luminescence could be separated from the broad ligand-centred $\pi^* \rightarrow \pi$ emission and provided mono-exponential decay values with characteristic $Er(^4S_{3/2})$ lifetimes of 38(4) ns for GaEr and 40(2) ns for GaErGa

at 3 K in the solid state (entries 5 and 6 in Table 1, Fig. 5b and S11‡).

In conclusion, the tight wrapping of the three bulky poly-aromatic N-heterocyclic tridentate binding units in the triple-helical $[GaLn(L1)_3](CF_3SO_3)_6$ and $[GaLnGa(L2)_3](CF_3SO_3)_9$ complexes produces compact, stable and inert nine-coordinate cavities for the lanthanide cations. For Ln = Er, the concomitant existence of a comparatively long-lived intermediate $Er(^4I_{13/2})$ excited state and of a short-lived, but emissive $Er(^4S_{3/2})$ excited state at higher-energy fulfils the two conditions required for the implementation of ETU in Er-containing molecular systems (Scheme 3). In a control experiment, direct continuous-wave laser excitation of the $Er(^4I_{9/2} \leftarrow {}^4I_{15/2})$ transition centred at λ_{exc} = 647 nm ($\bar{\nu}_{exc}$ = 15 454 cm^{-1}) failed to induce upconverted signals in the Ga/Er complexes (Fig. S12‡), which (i) confirmed Güdel's conclusion that there was little chance of detecting a single ion ESA in these molecular complexes,[7] and (ii) demonstrated that ligand-centred non-linear two-photon absorption processes did not compete efficiently with ETU under these conditions.

Optimizing the chromium coordination sphere for its use as a sensitizer in ETU processes with an erbium activator

Based on the specific photophysical properties of the Er^{III} activator implemented in $[MEr(L1)_3](CF_3SO_3)_6$ and $[MErM(L2)_3]$-$(CF_3SO_3)_9$, the associated M sensitizers should fit the following criteria: They should (1) replace Ga^{III} in order to yield a structurally-similar, kinetically inert and thermodynamically stable pseudo-octahedral $[MN_6]$ coordination building block, (2) possess a sensitizing excited state, the energy of which is in close resonance with one of the Er-centred excited state for maximizing M→Er energy transfer processes and (3) display a transparent optical window centred around 18 450 cm^{-1} in order to avoid the quenching by non-radiative energy transfer processes of the target upconverted emission arising from the $Er(^4S_{3/2})$ excited state.[11] Altogether, the trivalent chromium with its $[Ar]3d^3$ electronic configuration is a promising candidate since the energies of its six lower excited levels can be tuned by the ligand-field strength (measured by Δ in pseudo-octahedral complexes) and by the nephelauxetic effect (measured by the reduction of the Racah parameters B and C for electron–electron repulsion) produced by the terminal didentate benzimidazole-2-yl-pyridine binding units involved in the $[CrN_6]$ chromophores in $[CrLn(L1)_3](CF_3SO_3)_6$ and $[CrLnCr(L2)_3](CF_3SO_3)_9$ (eqn (S1)–(S6) in Fig. S13‡).[6] However, Cr^{III} is too inert to be used in a self-assembly process, and we therefore resorted to more labile Cr^{II} precursors followed by outer-sphere dioxygen oxidation for synthesizing $[CrLn(L1)_3]$-$(CF_3SO_3)_6$ and $[CrLnCr(L2)_3](CF_3SO_3)_9$ (Ln = Y, Er) complexes in 80–90% yields (Scheme 3 and Tables S1–S3‡). Orange X-ray quality prisms of $[CrYCr(L2)_3](CF_3SO_3)_9$ were found to be isostructural with $[GaErGa(L2)_3](CF_3SO_3)_9$, $[GaYGa(L2)_3](CF_3SO_3)_9$, $[CrEuCr(L2)_3](CF_3SO_3)_9$ and $[CrYbCr(L2)_3](CF_3SO_3)_9$.[11] The detailed analyses of the absorption and emission spectra recorded for $[CrY(L1)_3](CF_3SO_3)_6$ and $[CrYCr(L2)_3](CF_3SO_3)_9$ with the help of eqn (S1)–(S6) gave Δ = 20 130 cm^{-1}, B =
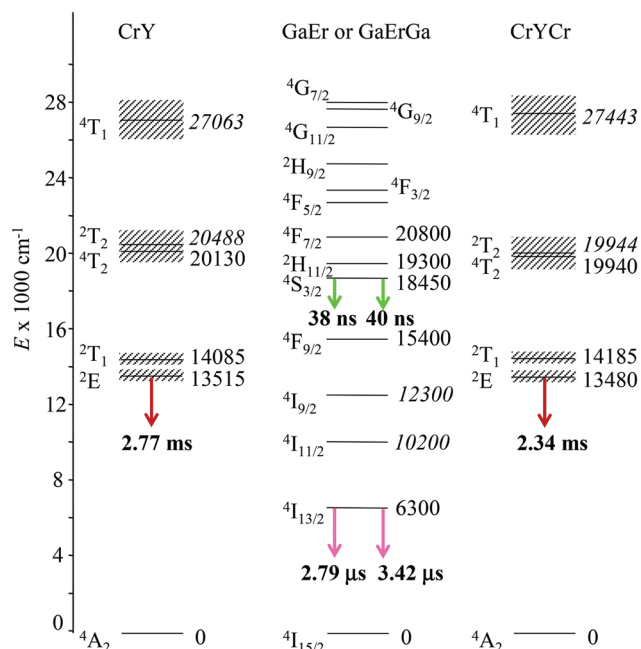
Fig. 6 Jablonski diagrams for the $[CrN_6]$ chromophores in $[CrY(L1)_3]$-$(CF_3SO_3)_6$ (left-hand side) and in $[CrYCr(L2)_3](CF_3SO_3)_9$ (right-hand side) and for the $[ErN_9]$ chromophores in $[GaEr(L1)_3](CF_3SO_3)_6$ and $[GaErGa-(L2)_3](CF_3SO_3)_9$ (centre). The energies of the excited levels deduced from the absorption, excitation and emission spectra are given with normal fonts, while the values obtained by computing are given in italics. The emissive levels are shown with full downward arrows mentioning their characteristic lifetimes in pure solids at 3–10 K.[11]

665 cm^{-1} and C = 2876 cm^{-1} for Cr^{3+} coordinated in the dinuclear complex, and Δ = 19 940 cm^{-1}, B = 736 cm^{-1} and C = 2737 cm^{-1} for Cr^{3+} in the trinuclear helicate (Fig. S13‡). These parameters are comparable to those found for pseudo-octahedral strong-field $[Cr(2,2'\text{-bipyridine})_3]^{3+}$ (Δ = 23 240 cm^{-1}, B = 761 cm^{-1} and C = 3044 cm^{-1}),[6] which indicates close locations of the didentate benzimidazole-pyridine and 2,2′-bipyridine binding units in the spectrochemical and nephelauxetic series.

The complete energy level diagram built for the $[CrN_6]$ and $[ErN_9]$ chromophores in Fig. 6 shows (i) a good match between the energy levels of the chromium sensitizer and those of the erbium activator for implementing efficient Cr(^{2}E)→Er(^{4}I$_{9/2}$) energy transfer processes in the target $[CrEr(L1)_3](CF_3SO_3)_6$ and $[CrErCr(L2)_3](CF_3SO_3)_9$ helicates, (ii) large Cr(^{4}T$_2$)–Cr(^{2}T$_1$) energy gaps compatible with the unquenched emission arising from the final Er(^{4}S$_{3/2}$) level and (iii) long luminescence lifetimes for the intermediate Cr(^{2}E) and Er(^{4}I$_{13/2}$) levels involved in the planned ETU process (Scheme 3). As expected, continuous-wave laser excitation of the Cr(^{2}E,^{2}T$_1$←^{4}A$_2$) transitions in the control compounds $[CrY(L1)_3](CF_3SO_3)_6$ and $[CrYCr(L2)_3]$-$(CF_3SO_3)_9$ (700 ≤ λ_{exc} ≤ 750 nm, 13 330 ≤ $\bar{\nu}_{exc}$ ≤ 14 280 cm^{-1}) failed to induce upconverted signals (Fig. S16a‡), which excludes the possibilities of Cr-centred upconversion processes or spurious ETU from impurities.[19]

Combining chromium sensitizers with erbium activators for the implementation of ETU processes in molecular complexes

In the triple-stranded dinuclear $[CrEr(L1)_3](CF_3SO_3)_6$ and trinuclear $[CrErCr(L2)_3](CF_3SO_3)_9$ complexes, the optimized nine-coordinated pseudo-tricapped $[ErN_9]$ chromophore is located at *ca.* 9 Å from one (dinuclear CrEr) or two (trinuclear CrErCr) strong-field $[CrN_6]$ sensitizers (see Fig. 5b). This intermetallic distance was designed for approaching the critical radius for 50% efficiency in the Cr→Er energy transfer,[10] a situation which maximizes the Cr-centred ETU mechanism operating in the trinuclear CrErCr complex (Fig. 7b, green trace).[11] Intermetallic communication *via* Cr(^{2}E)→Er(^{4}I$_{9/2}$) energy transfer is indeed evidenced by the 20–50% reduction of the Cr(^{2}E) excited lifetimes observed upon replacement of photophysically inactive Ln = Y (entries 1 and 2 in Table 1) with Ln = Er in CrLn and CrLnCr complexes (Fig. S14‡).[11] Assuming that the Cr→Er energy transfer is the only source of additional quenching of the Cr(^{2}E) excited state going from Ln = Y to Ln = Er, eqn (5) estimates the rate constants for Cr(^{2}E)→Er(^{4}I$_{9/2}$) energy transfers, which amount to $W_1^{Cr\rightarrow Er}$ = 295(5) s^{-1} for CrEr and 170(4) s^{-1} for CrErCr at 10 K (entry 9 in Table 1 and Fig. S15,‡ τ_{Cr} stand for the characteristic lifetimes of the Cr(^{2}E) levels measured in the various complexes).[11]

$$W_1^{Cr\rightarrow Er} = k_{Cr}^{obs}(Cr_nEr) - k_{Cr}^{1\rightarrow 0}(Cr_nY)$$
$$= [\tau_{Cr}(Cr_nEr)]^{-1} - [\tau_{Cr}(Cr_nY)]^{-1} \quad (5)$$

The resulting ETU mechanism proposed in Scheme 3 can be thus modelled with two simplified kinetic schemes (Fig. 7).[20] As suggested by these diagrams, NIR irradiation into the Cr(^{2}E,^{2}T$_1$←^{4}A$_2$) transitions at 700 ≤ λ_{exc} ≤ 750 nm (13 330 ≤ $\bar{\nu}_{exc}$ ≤ 14 280 cm^{-1}) indeed produced weak upconverted green emissions arising from the Er(^{4}S$_{3/2}$→^{4}I$_{15/2}$) transitions (Fig. S16a‡), while the experimental slopes of 1.7–2.0 reported for the log–log plot of the upconverted intensity with respect to the incident laser intensities confirmed the successive absorption of two photons (Fig. S16b‡).[11]

The complete set of kinetic rate constants collected in Table 1 allows us to further explore the ETU mechanisms operating in the dinuclear (Fig. 7a) and trinuclear (Fig. 7b) complexes. The macroscopic intensity measured for the final upconverted signal in CrEr and CrErCr is proportional to the normalized population density in the Er(^{4}S$_{3/2}$) excited state $N^{|Er(^4S_{3/2})\rangle}$ modulated by its intrinsic emission quantum yield $\phi_{lum}^{|Er(^4S_{3/2})\rangle}$. The ratio of the upconverted intensities recorded for the two complexes under similar experimental conditions $I_{Er}^{up}(CrErCr)/I_{Er}^{up}(CrEr)$ thus obeys eqn (6).[11]

$$\frac{I_{Er}^{up}(CrErCr)}{I_{Er}^{up}(CrEr)} = \frac{N^{|Er(^4S_{3/2})\rangle}(CrErCr)}{N^{|Er(^4S_{3/2})\rangle}(CrEr)} \cdot \frac{\phi_{lum}^{|Er(^4S_{3/2})\rangle}(CrErCr)}{\phi_{lum}^{|Er(^4S_{3/2})\rangle}(CrEr)} \quad (6)$$

Since the Er^{3+} cation is only slightly more accessible to high-energy vibrations in $[CrEr(L1)_3]^{6+}$ than in $[CrErCr(L2)_3]^{9+}$ (*vide supra*), one can reasonably assume that $\phi_{lum}^{|Er(^4S_{3/2})\rangle}(CrErCr) \approx \phi_{lum}^{|Er(^4S_{3/2})\rangle}(CrEr)$ and that therefore the
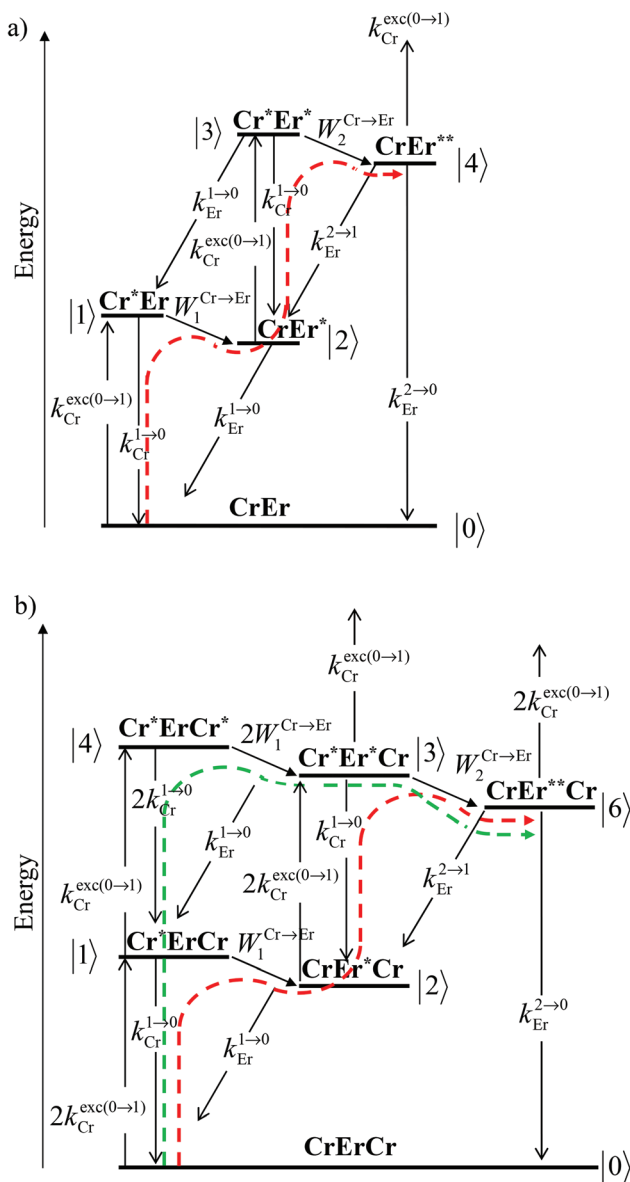
Fig. 7 Simplified kinetic schemes[20] depicting the modelling of energy transfer upconversion (ETU) processes occurring upon off-resonance irradiation into the sensitizer-centred absorption bands in (a) the dinuclear $[CrEr(L1)_3]^{6+}$ and (b) the trinuclear $[CrErCr(L2)_3]^{9+}$ complexes. $k_{Cr}^{exc(0\rightarrow1)}$ is the pumping rate constant for irradiation into the $Cr(^2T_1\leftarrow{}^4A_2)$ absorption band at λ_p = 705 nm (eqn (9)). $k_{Cr}^{1\rightarrow0}$, respectively $k_{Er}^{1\rightarrow0}$, $k_{Er}^{2\rightarrow1}$ and $k_{Er}^{2\rightarrow0}$ are the decay rate constants (i.e. the sum of radiative and non-radiative processes) for the $Cr(^2E\rightarrow{}^4A_2)$ transition in Cr_nY and for the $Er(^4I_{13/2}\rightarrow{}^4I_{15/2})$, $Er(^4S_{3/2}\rightarrow{}^4I_{13/2})$ and $Er(^4S_{3/2}\rightarrow{}^4I_{15/2})$ transitions in Ga_nEr, respectively. $W_1^{Cr\rightarrow Er}$ and $W_2^{Cr\rightarrow Er}$ are the rate constants of $Cr\rightarrow Er$ energy transfer processes. The red dashed pathways highlight the Er-centred ETU mechanism, while the green dashed pathway holds for the additional Cr-centred ETU mechanism operating in Cr_nEr when $n \geq 2$.[11]

ratio of intensities roughly corresponds to the ratio of the normalized population densities $N^{|Er(^4S_{3/2})\rangle}(CrErCr)/N^{|Er(^4S_{3/2})\rangle}(CrEr)$. Under Cr-centred excitation at a fixed incident pump intensity P, the pumping rate constant $k_{Cr}^{exc(0\rightarrow1)}$ is given by eqn (7), where λ_p is the pump wavelength, $\sigma_{Cr}^{0\rightarrow1}$ is the absorption cross

section of the $Cr(^2E,^2T_1\leftarrow{}^4A_2)$ transition, h is the Planck's constant and c is the vacuum speed of light.[22]

$$k_{Cr}^{exc(0\rightarrow1)} = \frac{\lambda_p}{hc}P\sigma_{Cr}^{0\rightarrow1} \qquad (7)$$

Assuming that all the kinetic rate constants involved in the kinetic diagrams depicted in Fig. 7 are in hand, the normalized population densities for each level can be computed with eqn (8), whereby M is the kinetic matrix associated with each kinetic diagram (Fig. S17–S18‡).[11,17]

$$\left[\frac{dN^{|i\rangle}}{dt}\right] = M \times \left[N^{|i\rangle}\right] \qquad (8)$$

The steady-state regime $dN^{|i\rangle}/dt = 0$ induced by the continuous-wave irradiation of the sensitizer reduces eqn (8) to $M \times [N^{|i\rangle}] = 0$, a situation 'easily' solved for $[N^{|i\rangle}]$ by using eqn (9), where M' is the rectangular matrix produced by the inclusion of mass conservation $\sum_i N^{|i\rangle} = N_{tot} = 1$ into the square kinetic matrix M ($^TM'$ is the transpose matrix, see Appendix 4‡ for mathematical details).[11]

$$\left[N^{|i\rangle}\right] = \left(^TM' \times M'\right)^{-1} \times {}^TM' \times \begin{bmatrix} 0 \\ \cdot \\ 0 \\ N_{tot} \end{bmatrix} \qquad (9)$$

The successive introduction of the rate constants gathered for $[CrEr(L1)_3](CF_3SO_3)_6$ and for $[CrErCr(L2)_3]$ $(CF_3SO_3)_9$ into eqn (9) provides the normalized population densities and their ratio $N^{|Er(^4S_{3/2})\rangle}(CrErCr)/N^{|Er(^4S_{3/2})\rangle}(CrEr)$ so that the two experimentally non-accessible parameters, i.e. the $Cr(^2E,^2T_1\leftarrow{}^4A_2)$ absorption cross sections $\sigma_{Cr}^{0\rightarrow1}$ required for computing $k_{Cr}^{exc(0\rightarrow1)}$ in eqn (7) and the rate constants for the second energy transfer process $W_2^{Cr\rightarrow Er}$ responsible for the $Er(^4S_{3/2}\leftarrow{}^4I_{13/2})$ superexcitation pathway, can be estimated. Assuming that (1) $\sigma_{Cr}^{0\rightarrow1}(CrEr) \approx \sigma_{Cr}^{0\rightarrow1}(CrErCr) = 10^{-24}$ m^2,[23] and (2) the trend in energy transfer processes experimentally observed for $W_1^{Cr\rightarrow Er}$ also holds for $W_2^{Cr\rightarrow Er}$ (i.e. $W_2^{Cr\rightarrow Er}(CrEr) = W_1^{Cr\rightarrow Er}(CrEr) = 295$ s^{-1} and $W_2^{Cr\rightarrow Er}(CrErCr) = W_1^{Cr\rightarrow Er}(CrErCr) = 170$ s^{-1}), we calculated $N^{|Er(^4S_{3/2})\rangle}(CrErCr)/N^{|Er(^4S_{3/2})\rangle}(CrEr) \approx 10$ (Fig. 8), in fair agreement with the experimental ratios of $I_{Er}^{up}(CrErCr)/I_{Er}^{up}(CrEr) =$ 4–10 reported for the upconverted intensities measured for the two complexes in the 10–50 K range (Fig. S16‡).[11] For large pump intensities (log(P) $\geq$ 1), the computed $I_{Er}^{up}(CrErCr)/I_{Er}^{up}(CrEr)$ ratio takes a downturn due to saturation effects affecting the Cr-centred ETU mechanism in the triad (Fig. 8b).

Conclusion

This work demonstrates that the photophysically active and kinetically inert Cr^{III} cations found in dinuclear $[CrLn(L1)_3]^{6+}$ and trinuclear $[CrLnCr(L2)_3]^{9+}$ triple-stranded helicates can be replaced with the closed-shell Ga^{III} to give slightly less inert, isostructural $[GaLn(L1)_3]^{6+}$ and trinuclear $[GaLnGa(L2)_3]^{9+}$ complexes, for which the photophysical properties of the
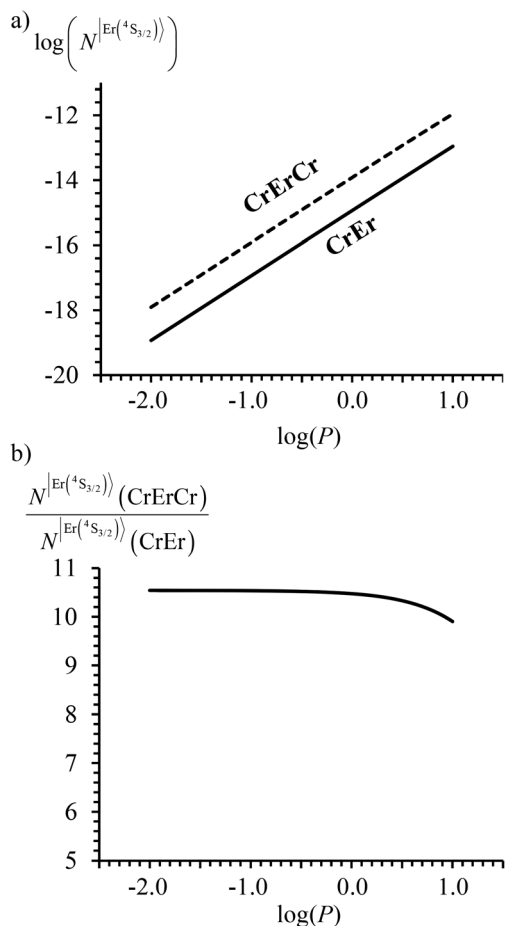
Fig. 8 (a) Log–log plot and (b) ratio of the quadratic dependence of the steady-state normalized population densities $N^{|Er(^4S_{3/2})\rangle}$ on the incident pump intensity (P in W mm^{-2}) computed for the dinuclear [CrEr(**L1**)$_3$]-(CF$_3$SO$_3$)$_6$ (the full trace) and for the trinuclear [CrErCr(**L2**)$_3$](CF$_3$SO$_3$)$_9$ (the dotted trace) complexes using eqn (9) and the kinetic rate constants gathered in Table 1. $\sigma_{Cr}^{0\to1}$(CrEr) $\approx \sigma_{Cr}^{0\to1}$(CrErCr) = 10^{-24} m^2,[23] $W_2^{Cr\to Er}$(CrEr) = $W_1^{Cr\to Er}$(CrEr) = 295 s^{-1} and $W_2^{Cr\to Er}$(CrErCr) = $W_1^{Cr\to Er}$(CrErCr) = 170 s^{-1} (see the text).

lanthanide cations can be deciphered without the complication due to the presence of the d-block cations. In this context, the pseudo-tricapped trigonal prismatic [ErN$_9$] chromophore appears to be exceptional in its capacity to simultaneously emit downshifted visible light arising from the Er($^4S_{3/2}$) level and near-infrared emission from the lowest Er($^4I_{15/2}$) excited level upon ligand-centred excitation, and this despite the presence of high-energy oscillators brought by the organic ligand strands. It is therefore not so surprising, but still remarkable, that the replacement of Er^{III} with either Tm^{III} (Fig. S19‡) or Ho^{III} (Fig. S20‡) in [GaLnGa(**L2**)$_3$]$^{9+}$ similarly produces rich lanthanide-centred luminescence upon UV-excitation of the aromatic receptor (Fig. S21‡). The combination of the [ErN$_9$] chromophore, acting as the activator, with optically-adapted strong-field pseudo-octahedral [CrN$_6$] sensitizers in [CrEr(**L1**)$_3$]$^{6+}$ and [CrErCr(**L2**)$_3$]$^{9+}$ complexes further tolerates radiative visible de-excitation of the Er($^4S_{3/2}$) level, and Cr-

centred NIR excitation induces light-upconversion obeying an ETU mechanism (Scheme 3). Such behaviour requires a collection of favourable conditions which are difficult to gather in a single entity and, despite efficient Cr(^2E)→Tm($^3H_4$) energy transfer processes observed in [CrTmCr(**L2**)$_3$]$^{9+}$ (Fig. S22‡), we were unable to detect chromium-to-thulium ETU (Fig. S23‡), probably because the target blue Tm($^1G_4\to^3H_6$) emission is quenched by an efficient Tm($^1G_4$)→Cr($^4T_2$) energy back-transfer (Fig. S21‡). For [CrHoCr(**L2**)$_3$]$^{9+}$, the poor energy match between the Cr(^2E) and Ho($^5I_5$) levels (Fig. S21‡) limits the Cr→Ho energy transfer rate constant to less than 100 s^{-1} (Fig. S22‡), and no upconversion could be evidenced upon Cr-centred excitation (Fig. S24‡). Finally, numerical simulations with eqn (9) show that using reasonable values for the various excited lifetimes in metallic sensitizers (in the millisecond range) and activators (in the microsecond range) involved in heterometallic M$_n$Ln (supra)molecular complexes, both Ln-centred (the red pathway in Fig. 7) and M-centred (the green pathway in Fig. 7) ETU mechanisms greatly benefit from the maximization of (i) the number n of sensitizers per activator and (ii) the rate constants for the second M→Ln energy transfer process ($W_2^{M\to Ln}$). As a test, a unique and common value for the intermetallic Cr→Er energy transfer rates constants in the CrEr and CrErCr complexes was considered for a comparison purpose. Introducing $W_2^{Cr\to Er}$(CrEr) = $W_1^{Cr\to Er}$(CrEr) = $W_2^{Cr\to Er}$(CrErCr) = $W_1^{Cr\to Er}$(CrErCr) = 170 s^{-1} into eqn (9) yields $N^{|Er(^4S_{3/2})\rangle}$(CrErCr)/$N^{|Er(^4S_{3/2})\rangle}$(CrEr) ≈ 220 (Fig. S25‡), a ratio which would have prevented the experimental detection of upconverted luminescence for the dinuclear CrEr helicate with our setup. The weak, but measurable upconverted signal experimentally recorded for the latter [CrEr(**L1**)$_3$]$^{6+}$ complex upon chromium-centred NIR excitation is thus indebted to the Cr→Er rate constant, $W^{Cr\to Er}$, which is twice as large as that measured in the trinuclear [CrErCr(**L2**)$_3$]$^{9+}$ analogue. Further optimization should therefore focus on the increase of $W_2^{M\to Ln}$ with the help of super-exchange mechanisms in polynuclear M$_n$Ln complexes.[24]

Experimental

Solvents and starting materials

These were purchased from Strem, Acros, Fluka AG and Aldrich and used without further purification unless otherwise stated. The trifluoromethanesulfonate salts Ln(CF$_3$SO$_3$)$_3$·xH$_2$O were prepared from the corresponding oxide (Aldrich 99.99%).[25] The synthesis of ligand **L1** is detailed in Appendix 1.‡ The ligand **L2**[26] and the complexes [MLn(**L1**)$_3$](CF$_3$SO$_3$)$_6$·x(H$_2$O)·y(C$_3$H$_5$N) and [MLnM(**L2**)$_3$](CF$_3$SO$_3$)$_9$·x(H$_2$O)·y(C$_3$H$_5$N) were prepared according to literature procedures (M = Cr, Ga and Ln = Ho, Tm, Er, Y using propionitrile as a solvent) and characterized by elemental analyses (Table S1‡) and single-crystal X-ray diffraction.[11] Acetonitrile and dichloromethane were distilled over calcium hydride.

Spectroscopic and analytical measurements

The details of the setup and procedures used for recording high-resolution emission spectra at variable temperatures under various excitation conditions are reported in ref. 11. Time-resolved luminescence spectra of $[GaEr(L1)_3](CF_3SO_3)_6$ and $[GaErGa(L2)_3](CF_3SO_3)_9$ were obtained from powder samples directly mounted onto copper plates using conductive silver glue, and cooled in an optical closed-cycle cryostat capable of reaching low temperatures down to 3 K under a helium atmosphere (Sumitomo SHI-950/Janis Research CCS-500/204). High-resolution emission spectra were recorded upon excitation with Nd:YAG lasers (Quantel Brilliant B) by using the third harmonic at 355 nm. The laser was connected to a gated CCD detector (Andor iSTAR) during the monitoring of the luminescence spectra. The emitted light was analysed at 90° using an Andor SR-163 monochromator (slits 100 μm) with a holographic grating (600 grooves mm^{-1}, blazed at 500 nm). Appropriate filters (395 or 435 nm cutoff) were used to remove the residual excitation laser light, the Rayleigh scattered light and associated harmonics from the emission spectra. A kinetic series was recorded using a gate pulse width of 15 ns and by scanning the delay from just before the arrival of the laser pulse to 350 ns in steps of 10 ns. Each spectrum corresponds to the sum of 1200–5000 scans. All the luminescence spectra were transferred to a PC for data analysis. The intensity at 541 nm and the integrated intensity between 535 and 560 nm corresponding to the $Er(^4S_{3/2} \rightarrow {}^4I_{15/2})$ transition were calculated for each curve after background correction of the ligand-centred emission. The maximum intensity and the integrated intensity *vs.* the time (0–350 ns) were plotted, from which the characteristic lifetimes for the $Er(^4S_{3/2})$ level could be estimated. ^1H and ^{13}C NMR spectra were recorded at 293 K on a BrukerAvance 400 MHz spectrometer. Chemical shifts are given in ppm with respect to tetramethylsilane $Si(CH_3)_4$. Pneumatically-assisted electrospray (ESI) mass spectra were recorded from 10^{-4} M solutions on an Applied Biosystems API 150EX LC/MS System equipped with a Turbo Ionspray source®. Elemental analyses were performed by K. L. Buchwalder from the Microchemical Laboratory of the University of Geneva. Electronic absorption spectra in the UV-Vis were recorded at 20 °C from solutions with a Perkin-Elmer Lambda 900 spectrometer using quartz cells of 10 or 1 mm path length. The mathematical analyses were performed by using Igor Pro® (WaveMetrics Inc.) and Excel® (Microsoft) softwares.

X-Ray crystallography

Fragile crystals of $[GaErGa(L2)_3](CF_3SO_3)_9(CH_3CN)_{35.5}$ (**16**) were obtained by slow diffusion of *tert*-butylmethylether into an acetonitrile solution of $[GaErGa(L2)_3]^{9+}$, while those of $[CrEr(L1)_3](CF_3SO_3)_6(C_3H_5N)_{26}$ (**17**) were obtained by the slow diffusion of *tert*-butylmethylether into a concentrated propionitrile solution of $[CrEr(L1)_3]^{6+}$. As the crystals did not survive when separated from their mother liquors, we deposited the crystals on a filter paper, briefly sucked the excess solvent

under vacuum and dissolved the resulting materials into CD_3CN. The ^1H NMR spectra showed the presence of the $[GaErGa(L2)_3]^{9+}$, resp. $[CrEr(L1)_3]^{6+}$ cations together with acetonitrile and the resp. propionitrile molecules, but no signal for the heavy ether. It was therefore assumed that the crystals contained $[GaErGa(L2)_3](CF_3SO_3)_9$ and $[CrEr(L1)_3]$-$(CF_3SO_3)_6$ together with nitrile solvent molecules. Summaries of crystal data, intensity measurements and structure refinements for $[GaErGa(L2)_3](CF_3SO_3)_9(CH_3CN)_{35.5}$ (**16**) and $[CrEr$-$(L1)_3](CF_3SO_3)_6(C_3H_5N)_{26}$ (**17**) are collected in Tables S4 and S9 (ESI‡). Each crystal was mounted on a kapton loop with protection oil. Cell dimensions and intensities were measured at 150 K on an Agilent Supernova diffractometer with mirror-monochromated $Cu[K\alpha]$ radiation (λ = 1.54 187) for **16** or at 100 K using the Swiss-Norwegian beamlines, European Synchtron Radiation Facility (λ = 0.8231 Å) for **17**. Data were corrected for Lorentz and polarization effects and for absorption. The structure was solved by direct methods (SIR97),[27] and all other calculations were performed with ShelX97[28] systems and ORTEP[29] programs. CCDC-1003567 and CCDC-1003568 contain the supplementary crystallographic data.

Warning. The quality of the diffraction data and their refinement is low due to considerable disorder. For **16**, twelve triflate anions could be located and refined, but the absence of features that could be unambiguously attributed to the missing six triflate anions and to the solvent molecules in the Fourier difference map forced us to apply the Squeeze/bypass method (program PLATON) in order to take care of the remaining electronic density. There is a huge void in the structure, in which 2003 electrons per formula unit were attributed to Squeeze. This corresponded to six triflates together with 71 acetonitrile molecules which were included in the unit cell. In **17**, the six $CF_3SO_3^-$ counter-anions and interstitial solvent molecules were highly disordered in large voids in the structure. In the absence of diagnostic features in the Fourier difference map, the Squeeze/bypass method (program PLATON)[30] was used to take care of the remaining electron density, which was eventually assigned to six triflates and 26 propionitrile molecules (details are given in the associated CIF file).

Acknowledgements

Notes and references

1 (*a*) *Nonlinear Optical Properties of Organic Molecules and Crystals*, ed. D. S. Chemla and J. Zyss, Academic Press,

Orlando, 1987; (b) P. N. Prasad and D. J. Williams, *Introduction to Nonlinear Optical Effects in Molecules and Polymers*, John Wiley & Sons, Inc., New York, 1991; (c) J. Zyss, *Molecular Nonlinear Optics: Materials, Physics and Devices*, Academic Press, Boston, 1994; (d) *Nonlinear Optics of Organic Molecules and Polymers*, ed. H.S. Nalwa and S. Miyata, CRC Press, Boca Raton, 1997.

2 (a) F. Terenziani, C. Katan, E. Badaeva, S. Tretiak and M. Blanchard-Desce, *Adv. Mater.*, 2008, **20**, 4641–4678; (b) C. Andraud and O. Maury, *Eur. J. Inorg. Chem.*, 2009, 4357–4371; (c) P. Neveu, D. K. Sinha, P. Kettunen, S. Vriz, L. Jullien and D. Bensimon, *Springer Ser. Chem. Phys.*, 2010, **96**, 305–316; (d) A. D'Aléo, A. Bourdolle, S. Brustlein, T. Fauquier, A. Grichine, A. Duperray, P. L. Baldeck, C. Andraud, S. Brasselet and O. Maury, *Angew. Chem., Int. Ed.*, 2012, **51**, 6622–6625.

3 (a) S. V. Eliseeva and J.-C. G. Bünzli, *New J. Chem.*, 2011, **35**, 1165–1176; (b) X. Huang, S. Han, W. Huang and X. Liu, *Chem. Soc. Rev.*, 2013, **42**, 173–201; (c) J.-C. G. Bünzli and A.-S. Chauvin, in *Handbook on the Physics and Chemistry of Rare Earths*, ed. J.-C. G. Bünzli and V. K. Pecharsky, Elsevier, North Holland, Amsterdam, 2014, vol. 44, pp. 169–281.

4 (a) T. N. Singh-Rachford and F. N. Castellano, *Coord. Chem. Rev.*, 2010, **254**, 2560–2573; (b) J. Zhao, S. Ji and H. Guo, *RSC Adv.*, 2011, **1**, 937–950; (c) A. Monguzzi, R. Tubino, S. Hoseinkhani, M. Campione and F. Meinardi, *Phys. Chem. Chem. Phys.*, 2012, **14**, 4322–4332; (d) J.-H. Kim, F. Deng, F. N. Castellano and J.-H. Kim, *Chem. Mater.*, 2012, **24**, 2250–2252; (e) X. Huang, S. Han, W. Huang and X. Liu, *Chem. Soc. Rev.*, 2013, **42**, 173–201.

5 (a) F. Auzel, *Chem. Rev.*, 2004, **104**, 139–173; (b) B. M. van der Ende, L. Aarts and A. Meijerink, *Phys. Chem. Chem. Phys.*, 2009, **11**, 11081–11095; (c) M. Haase and H. Schäfer, *Angew. Chem., Int. Ed.*, 2011, **50**, 5808–5829.

6 L. Aboshyan-Sorgho, M. Cantuel, S. Petoud, A. Hauser and C. Piguet, *Coord. Chem. Rev.*, 2012, **256**, 1644–1663.

7 C. Reinhard and H. U. Güdel, *Inorg. Chem.*, 2002, **41**, 1048–1055.

8 O. A. Blackburn, M. Tropiano, T. J. Sorensen, J. Thom, A. Beeby, L. M. Bushby, D. Parker, L. S. Natrajan and S. Faulkner, *Phys. Chem. Chem. Phys.*, 2012, **14**, 13378–13384.

9 H. Suzuki, Y. Nishida and S. Hoshino, *Mol. Cryst. Liq. Cryst.*, 2003, **406**, 27/[221]–237/[231].

10 L. Aboshyan-Sorgho, C. Besnard, P. Pattison, K. R. Kittilstved, A. Aebischer, J.-C. G. Bünzli, A. Hauser and C. Piguet, *Angew. Chem., Int. Ed.*, 2011, **50**, 4108–4112.

11 Y. Suffren, D. Zare, S. V. Eliseeva, L. Guénée, H. Nozary, T. Lathion, L. Aboshyan-Sorgho, S. Petoud, A. Hauser and C. Piguet, *J. Phys. Chem. C*, 2013, **117**, 26957–26963.

12 (a) G. A. Kumar, R. Riman, S. C. Chae, Y. N. Jang, I. K. Bae and H. S. Moon, *J. Appl. Phys.*, 2004, **95**, 3243–3249; (b) A. K. Singh, S. B. Rai, D. K. Rai and V. B. Singh, *Appl.*

Phys. B, 2006, **82**, 289–294; (c) F. Prudenzano, L. Mescia, L. Allegretti, V. Moizan, V. Nazabal and F. Smektala, *Opt. Mater.*, 2010, **33**, 241–245.

13 (a) J. W. Hofstraat, M. P. Oude Wolbers, F. C. J. M. Van Veggel, D. N. Reinhoudt, M. H. V. Werts and J. W. Verhoeven, *J. Fluoresc.*, 1998, **8**, 301–308; (b) M. P. Oude Wolbers, F. C. J. M. van Veggel, F. G. A. Peters, E. S. E. van Beelen, J. W. Hofstraat, F. A. J. Geurts and D. N. Reinhoudt, *Chem. – Eur. J.*, 1998, **4**, 772–780; (c) L. H. Sloof, A. Polman, M. P. O. Wolbers, F. C. J. M. van Veggel, D. N. Reinhoudt and J. W. Hofstraat, *J. Appl. Phys.*, 1998, **83**, 497–503; (d) B. M. Flanagan, P. V. Bernhardt, E. R. Krausz, S. R. Lüthi and M. J. Riley, *Inorg. Chem.*, 2001, **40**, 5401–5407; (e) K. Kuriki, Y. Koike and Y. Okamoto, *Chem. Rev.*, 2002, **102**, 2347–2356; (f) L. H. Sloof, A. van Blaaderen, A. Polman, G. A. Hebbink, S. I. Klink, F. C. J. M. Van Veggel, D. N. Reinhoudt and J. W. Hofstraat, *J. Appl. Phys.*, 2002, **91**, 3955–3980; (g) V. S. Sastri, J.-C. Bünzli, V. R. Rao, G. V. S. Rayudu and J. R. Perumareddi, *Modern Aspects of Rare Earths and Their Complexes*, Elsevier, Amsterdam, 2003, ch. 8, pp. 629–632; (h) S. Quici, G. Marzanni, A. Forni, G. Accorsi and F. Barigelletti, *Inorg. Chem.*, 2004, **43**, 1294–1301; (i) G. M. Davies, H. Adams, S. J. A. Pope, S. Faulkner and M. D. Ward, *Photochem. Photobiol. Sci.*, 2005, **4**, 829–834; (j) G. Mancino, A. J. Ferguson, A. Beeby, N. J. Long and T. S. Jones, *J. Am. Chem. Soc.*, 2005, **127**, 524–525; (k) J. B. Oh, Y. H. Kim, M. K. Nah and H. K. Kim, *J. Lumin.*, 2005, **111**, 255–264; (l) M.-K. Nah, H.-G. Cho, H.-J. Kwon, Y.-J. Kim, C. Park, H. K. Kim and J.-G. Kang, *J. Phys. Chem. A*, 2006, **110**, 10371–10374; (m) S. Destri, M. Pasini, W. Porzio, F. Rizzo, G. Dellepiane, M. Ottonelli, G. Musso, F. Meinardi and L. Veltri, *J. Lumin.*, 2007, **127**, 601–610; (n) X. Li, Z. Si, C. Pan, L. Zhou, Z. Li, X. Li, J. Tang and H. Zhang, *Inorg. Chem. Commun.*, 2009, **12**, 675–677; (o) F. Artizzu, M. L. Mercuri, A. Serpe and P. Deplano, *Coord. Chem. Rev.*, 2011, **255**, 2514–2529; (p) D. J. Lewis, F. Moretta, A. T. Holloway and Z. Pikramenou, *Dalton Trans.*, 2012, **41**, 13138–13146; (q) P. Martin-Ramos, C. Coya, A. L. Alvarez, M. Ramos Silva, C. Zaldo, J. A. Paixao, P. Chamorro-Posada and J. Martin-Gil, *J. Phys. Chem. C*, 2013, **117**, 10020–10030.

14 (a) C. Piguet, J.-C. G. Bünzli, G. Bernardinelli and A. F. Williams, *Inorg. Chem.*, 1993, **32**, 4139–4149; (b) C. Piguet, J.-C. G. Bünzli, G. Bernardinelli, C. G. Bochet and P. Froidevaux, *J. Chem. Soc., Dalton Trans.*, 1995, 83–97; (c) S. Petoud, J.-C. G. Bünzli, F. Renaud, C. Piguet, K. J. Schenk and G. Hopfgartner, *Inorg. Chem.*, 1997, **36**, 5750–5760.

15 (a) C. Piguet, E. Rivara-Minten, G. Hopfgartner and J.-C. G. Bünzli, *Helv. Chim. Acta*, 1995, **78**, 1541–1566; (b) C. Piguet, J.-C. G. Bünzli, G. Bernardinelli, G. Hopfgartner, S. Petoud and O. Schaad, *J. Am. Chem. Soc.*, 1996, **118**, 6681–6697.

16 D. Lavabre, V. Pimienta, G. Levy and J. C. Micheau, *J. Phys. Chem.*, 1993, **97**, 5321–5326.

17 M. E. Starzak, *Mathematical Methods in Chemistry and Physics*, Plenum press, New York, 1989, pp. 289–357.

18 Because of the intense visible luminescence of [GaEuGa-(L2)$_3$](CF$_3$SO$_3$)$_9$, the Er salts used for preparing [GaErGa-(L2)$_3$](CF$_3$SO$_3$)$_9$ must have the highest possible purity. Er$_2$O$_3$ (99.99%) provided the emission spectrum depicted in Fig. 5 (the blue trace), but the use of Er$_2$O$_3$ (99.9%) showed concomitant Er- and Eu-centred emissions at low temperature (Fig. S10b‡).

19 O. S. Wenger, H. Güdel and S. Kück, *J. Chem. Phys.*, 2002, **117**, 909–913.

20 For the sake of clarity, the kinetic diagrams collected in Fig. 7 are limited to the lower excited states involved for two successive Cr-centred excitations. However, all calculations take into account the complete schemes described in ref. 11, which are reproduced in Fig. S17a–S18a‡ for the convenience of the reader.

21 S. Georgescu and V. Lupei, *J. Quantum Electron.*, 1998, **34**, 1031–1040.

22 M. Pollnau, D. R. Gamelin, S. R. Lüthi and H. U. Güdel, *Phys. Rev. B: Condens. Matter*, 2000, **61**, 3337–3346.

23 The absorption cross section $\sigma^{i \to j}$ (in cm^2) is related to the molar extinction coefficient $\varepsilon^{i \to j}$ (in m^{-1} cm^{-1}) by using $\sigma^{i \to j} = 3.8 \times 10^{-21} \cdot \varepsilon^{i \to j}$. Typical values of $\sigma_{Cr} \approx 10^{-24}$ m^2 have been reported in ref. 19 for the Cr(^{2}T$_1$,^{2}E←^{4}A$_2$) transitions observed for Cr^{3+} doped in Cs$_2$NaScCl$_6$.

24 M. E. von Arx, E. Burattini, A. Hauser, L. van Pieterson, R. Pellaux and S. Decurtins, *J. Phys. Chem. A*, 2000, **104**, 883–893.

25 J. F. Desreux, in *Lanthanide Probes in Life, Chemical and Earth Sciences*, ed. G. Choppin and J.-C. G. Bünzli, Elsevier, Amsterdam, 1989, ch. 2.

26 C. Piguet, B. Bocquet and G. Hopfgartner, *Helv. Chim. Acta*, 1994, **77**, 931–942.

27 A. Altomare, M. C. Burla, M. Camalli, G. Cascarano, C. Giacovazzo, A. Guagliardi, G. Moliterni, G. Polidori and R. Spagna, *J. Appl. Crystallogr.*, 1999, **32**, 115–119.

28 G. M. Sheldrick, *SHELXL97 Program for the Solution and Refinement of Crystal Structures*, University of Göttingen, Germany, 1997.

29 ORTEP3 for Windows. L. J. Farrugia, *J. Appl. Crystallogr.*, 1997, **30**, 565.

30 P. Van der Sluis and A. L. Spek, *Acta Crystallogr., Sect. A: Fundam. Crystallogr.*, 1990, **46**, 194–201.